



Zhang, T., Qiao, G., Smith, D.A. , Barakos, G.N. and Kusyumov, A. (2021) Parametric study of aerodynamic performance of equivalent ducted/un-ducted rotors. *Aerospace Science and Technology*, 117, 106984. (doi: [10.1016/j.ast.2021.106984](https://doi.org/10.1016/j.ast.2021.106984))

The material cannot be used for any other purpose without further permission of the publisher and is for private use only.

There may be differences between this version and the published version. You are advised to consult the publisher's version if you wish to cite from it.

<http://eprints.gla.ac.uk/246987/>

Deposited on 16 July 2021

Enlighten – Research publications by members of the University of
Glasgow

<http://eprints.gla.ac.uk>

Parametric Study of Aerodynamic Performance of Equivalent Ducted/Un-ducted Rotors

T. Zhang,^{*} G. Qiao,[†] D. A. Smith,[‡] G. N. Barakos,[§] and A. Kusyumov[¶]

This paper presents the performance analysis and a parametric study of equivalent ducted/un-ducted rotors using high-fidelity CFD methods. A model-scale ducted rotor case by NASA was analysed and used as the initial design. An equivalent un-ducted rotor producing the same thrust and power was first derived using the momentum theory. The ducted/un-ducted configurations were later scaled to support a four-rotor vehicle of 6,000 kg using a BEMT model. High-fidelity CFD simulations of the scaled designs were then performed. Far-field acoustics of the two configurations was also examined using the FW-H equations. Compared to the equivalent open rotor, the ducted rotor had a significantly reduced frontal area and was also able to deliver the desired thrust at lower torque and reduced noise, but the power was higher due to the higher RPM. A parametric study was then performed in hover and in forward flight to study the performance trends subject to variations of tip speed, blade pitch, blade radius, chord, twist, and duct thickness. Kriging surrogate models were constructed to provide an impression of the performance response to the particular design change. Both configurations showed similar responses to most design variables, but the sensitivity was different between configurations and between flight conditions. Detailed analyses of the parametric results are presented to guide ducted rotor designs.

Nomenclature

Latin

A = Area, m^2

C = Chord Length, m

C_{F_x} = Axial/Propulsion Force Coefficient, $C_{F_x} = F_x / (0.5 \rho_\infty V_\infty^2 S_{dp})$

C_{M_x} = Axial Moment Coefficient, $C_{M_x} = M_x / (0.5 \rho_\infty V_\infty^2 S_{dp} C)$

C_T = Thrust Coefficient, $C_T = T / (0.5 \rho V_{tip}^2 A_{disk})$

C_P = Power Coefficient, $C_P = P / (0.5 \rho V_{tip}^3 A_{disk})$

^{*}PhD Student, School of Engineering, University of Glasgow, G12 8QQ, UK

[†]MSc Student, School of Engineering, University of Glasgow, G12 8QQ, UK

[‡]Research Assistant, School of Engineering, University of Glasgow, G12 8QQ, UK

[§]Professor, School of Engineering, University of Glasgow, G12 8QQ, UK

[¶]Professor, Kazan National Research Technical University, Kazan, Russian Federation

F_x = Axial Force, N
 FoM = Figure of Merit, $FoM = (C_T)^{\frac{3}{2}}/(2C_P)$
 Ma = Mach Number
 M_x = Axial Moment, Nm
 N = Number of Blades
 SPL = Sound Pressure Level, $SPL = 20\log_{10}(rms(p')/p_{ref})$
 P = Power, W
 p' = Sound Pressure, Pa
 p_{ref} = Acoustic Reference Pressure, $p_{ref} = 2 \times 10^{-5}[Pa]$
 Q = Torque, Nm
 R = Blade Radius, m
 Re = Reynolds Number
 RPM = Revolutions Per Minute
 S_{dp} = Ducted Rotor Reference Area, $S_{dp} = C_{dp}D_{dp}, m^2$
 T = Thrust, N
 V = Flow Velocity, m/s

Greek

Λ = Duct Expansion Ratio, $\Lambda = A_{exit}/A_{disk}$
 μ = Advance Ratio, $\mu = V_{\infty}/V_{tip}$
 η = Froude/Propulsive Efficiency, $\eta = TV_{\infty}/(Q\Omega)$
 Ω = Rotational Speed, rad/s
 σ = Solidity, $\sigma = NC/(\pi R)$

Subscripts and superscripts

∞ = Free-stream Value
 dp = Ducted Rotor
 op = Open Rotor

Acronyms

FW-H = Ffowcs Williams-Hawkings
HMB3 = Helicopter Multi-Block 3

I. Introduction

There has been a surge in Urban Aerial Mobility (UAM) research and development in recent years [1], dominated by novel aircraft configurations and Electrical Vertical Take-Off and Landing (eVTOL). For the propulsion system, many UAM prototypes or conceptual designs have used electricity-driven and distributed propellers, while few have chosen ducted propellers, e.g. the Airbus CityAirbus and the Bell Nexus eVTOL. Indeed, the ducted rotor/propeller can be a very favourable choice of propulsion for future UAMs fulfilling the stringent efficiency and emission requirements. Comparing to conventional open propellers, the ducted propeller has very promising improvements in terms of aerodynamic efficiency, acoustic reduction, and safety. Of course, the ducting brings certain penalties. For instance, the duct contributes to drag rather than thrust at high advance ratios. Further, at large cross-wind angles or in edge-wise flight, the duct may suffer from flow separation, if not properly designed. Issues regarding duct weight, structural complexity, and vibration, should also be carefully considered. These advantages and disadvantages of the ducting need to be evaluated more quantitatively for modern aeronautical applications. A detailed review of ducted rotor research, including experiments, numerical simulations/optimisation, and research challenges, can be found in Ref. [2].

Experiments on ducted propellers can be dated back to the early years of aviation. In particular, extensive tests were conducted by NASA [3–5] in the 1960s and 1970s, during the development of two tilt-duct prototypes, the Bell X22 and the Doak VZ4D. Many of these tests used large, real-scale ducted rotor models, and were well documented, but focused on the performance of specific designs. Recent experimental studies [6–8] mostly aimed at Unmanned/Micro Aerial Vehicle (UAV/MAV) applications, hence the Reynolds numbers were small and the compressibility effects were only minor. Moreover, few tests disclosed their detailed geometric definitions and test data due to commercial restrictions. Nonetheless, most tests showed the higher efficiency of the ducted rotor at lower advance ratios with the extra thrust contributed by the duct surface. A few acoustic tests [9][10] also examined the noise reduction due to ducting. The acoustic patterns and strength were shown to be greatly altered by ducting the rotor.

Theoretical or lower-order numerical studies on ducted rotors can also be found. Particularly, Drela et.al [11, 12] presented an open-source code DFDC (Ducted Fan Design Code) based on extensions of classic lifting line theory and panel methods. Previous tests and comparisons [13] show that the code is capable of accurate and rapid thrust predictions for ducted propellers in axial flight, but the torque is generally over-predicted. More recently, Bontempo and Manna [14] presented exact solutions of incompressible, axisymmetric and inviscid flow through the duct through a non-uniform actuator disk. In general, these methods can give rapid predictions of ducted rotor performance but lack quantitatively agreement with test data due to their stringent assumptions, e.g. axial symmetry, incompressibility.

High-fidelity Computational Fluid Dynamics (CFD) methods can offer more accurate and delicate analyses of ducted rotor performance and flow fields. Unsteady Reynolds Averaged Navier-Stokes (URANS) simulations of ducted rotor flows were carried out by Jimenez and Singh et.al. [15] and by Biava and Barakos [16], more recently. Zhang and Barakos later [13] carried out extensive RANS/URANS simulations on the test case by Grunwald and Goodson [4].

Very favourable agreement with test data was noted, and large variations of operating conditions were investigated. Numerical optimisation of the ducted rotor designs can also be noted [16, 17]. However, due to geometries, relative motions, and complex flow features, the high-fidelity CFD modelling of ducted rotors with blades resolved remains challenging. Moreover, many simulations were performed on small-scale geometries for UAV/MAV applications and often lacked backing from experiments.

To further evaluate the usage of ducted rotors for future UAMs, more quantitative investigations of large-size ducted rotors performance and comparisons with conventional open rotors are necessary. Previous experimental or numerical studies generally lacked the systematic study of large-size designs and comparisons with equivalent open rotors. Compared to experimental and theoretical/lower-order tools, CFD represents a more suitable approach for the systematic or parametric investigation, combining accurate predications of performance and flow fields, and the flexibility to vary design and operating conditions.

The objectives of the current work are to study the performance of a large-size ducted rotor in a parametric way, and to compare with equivalent open rotors. A NASA ducted rotor design was chosen as the initial design and scaled to support a four-rotor vehicle of 6,000 kg. An open rotor design producing the equivalent amount of thrust and power to the ducted rotor configuration is proposed based on the momentum theory analysis. High-fidelity CFD simulations were performed to analyse the performance of the two baseline designs in hover, axial flight, and yawed conditions. Far-field acoustics was also evaluated based on the FW-H equations. The aerodynamic performance changes with respect to variations in 6 design parameters were later systematically examined. Kriging surrogate models were also built to provide an impression of the response to the particular design change.

II. Description of Test Cases

The present study is carried out using the ducted rotor geometry of Grunwald & Goodson [4] as the baseline design. This ducted rotor geometry was chosen due to the availability of existing data on its performance and geometry allowing for evaluation of the computational model. The baseline geometry of the Grunwald ducted rotor is shown in Figure 1. Details of the rotor blade geometry can be found in references [4] and [13]. This case was studied earlier by the authors and detailed CFD validation is reported in Ref. [13].

A. The ‘Equivalent’ Rotor

To compare the relative performance between open and ducted configurations, the concept of the ‘*equivalent*’ rotor is introduced. The momentum theory was used to derive the equivalent rotors between open and ducted configurations. The equivalent rotor is derived under hover conditions.

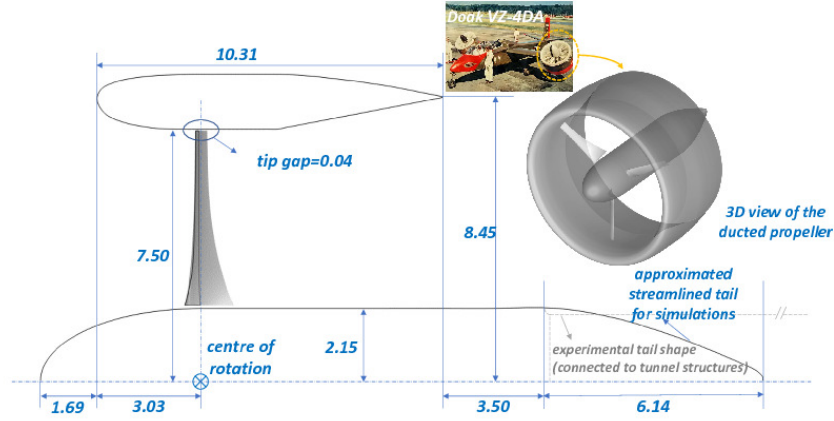


Fig. 1 Key parameters of the Grunwald ducted rotor geometry. Dimensions are in inches. Note the aft section of the *centrebod*y has been simplified for the purposes of the CFD simulations.

Firstly, considering the open rotor, from the momentum theory the thrust of an open rotor in hover is:

$$T_{op} = \dot{m}V_3 \quad (1)$$

where V_3 is the velocity far downstream equal to twice the induced velocity at the disk. The mass flow is $\dot{m} = \rho A_{op} v_i$, with v_i being the induced velocity at the rotor disk and A_{op} being the rotor disk area. Therefore:

$$T_{op} = 2\rho A_{op} v_i^2 \quad (2)$$

as from the conservation of energy, the rotor power is:

$$P_{op} = \frac{1}{2} \dot{m} V_3^2 = 2\rho A_{op} v_i^3 \quad (3)$$

Rearranging Equation (2) in terms of induced velocity, the open rotor power can be related to its thrust using:

$$P_{op} = \frac{T_{op}^{3/2}}{\sqrt{2\rho A_{op}}} \quad (4)$$

As for the ducted configuration in hover, the total thrust (i.e. duct plus rotor contributions) is given

$$\text{by: } T_{dp} = \dot{m}V_3 \quad (5)$$

where V_3 in this case is the flow velocity at the duct diffuser exit. The mass flow at the rotor disk is $\dot{m} = \rho A_{dp} v_i$, with

A_{dp} being the rotor disk area. From continuity, the velocity at the duct exit V_3 is related to the induced velocity v_i :

$$v_i A_{dp} = V_3 A_3 \implies V_3 = \frac{v_i}{\Lambda} \quad (6)$$

Here, A_3 is the area of the duct diffuser exit and Λ is the duct exit area ratio (A_3/A_{dp}) and is assumed constant. The thrust of the ducted rotor is then:

$$T_{dp} = \rho A_{dp} \Lambda v_i^2 \quad (7)$$

From the conservation of energy, the power of the ducted rotor is:

$$P_{dp} = \frac{1}{2} \dot{m} V_3^2 = \frac{1}{2} \Lambda^2 \rho A_{dp} v_i^3 \quad (8)$$

and rearranging Equation (7) in terms of induced velocity, the ducted rotor power can be related to its thrust using:

$$P_{dp} = \frac{T_{dp}^{3/2}}{\sqrt{4\Lambda\rho A_{dp}}} \quad (9)$$

The equivalent rotor is found when the power and thrust of both systems are equal, i.e. the same propulsive efficiency. Equating Equations (4) and (9), the blade radius correlation between the equivalent open and ducted rotors is found:

$$R_{dp} = \frac{R_{op}}{\sqrt{2\Lambda}} \quad (10)$$

B. Rotor Scaling

To ensure the results of the parametric study are relevant to modern multi-rotor concepts, the baseline design was scaled to provide a realistic rotor loading. For the scaling, a four-rotor vehicle of 6,000 kg mass was used to be representative of modern concepts. This weight is representative of a current medium to large utility helicopter. [This realistic size is also a good challenge for the current scaling and simulation methods due to the compressibility effects and high Reynolds number.](#) Hover conditions were used for scaling as these represent the most demanding conditions for the vehicle. In hover, the proposed vehicle would require a total thrust of 58,860N. Using a load factor of 1.2, this requires each rotor to deliver a total thrust of 17,658 N. [This allows for good manoeuvrability for a multi-rotor aircraft.](#)

A Blade Element Momentum Theory (BEMT) model was used to calculate the required scaling to deliver the required thrust for the vehicle. The scaling was carried out at constant tip speed, as used in the baseline design $Ma_{tip} = 0.468$. The scaling analysis was constrained to a range of 1 to 4m for the tip radius. The scaling was carried out on both open and ducted rotors. A preliminary analysis showed that a open rotor radius of $R = 3.75m$ and an equivalent ducted rotor of $R = 2.5m$ radius met the required performance. However, the blade count had to be increased

to 4 (from the baseline of 3) to obtain a pair of equivalent rotor configurations that met the loading constraints. The increase in blade count resulted in an increased solidity for the scaled rotors. However, the solidity remained equal for both configurations at $\sigma = 0.1834$.

Figure 2 compares the equivalent open and ducted rotors. Comparing the configurations shows that the computed equivalent ducted rotor configuration, including the duct surface, offers a significant reduction in frontal area for delivering the same thrust in comparison to the open rotor configuration. The analysis in the present work sets to quantify the benefits of the equivalent ducted rotor configuration of Figure 2.

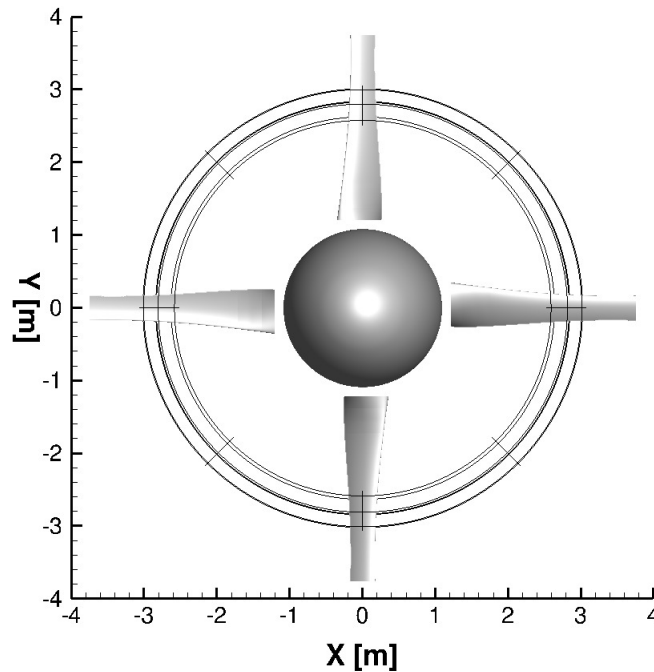


Fig. 2 Comparison of equivalent open and ducted rotors. The ducted rotor is shown using black outlines.

C. Parametric Study

In addition to comparing the baseline equivalent open and ducted rotor configurations, a parametric study was carried out to allow further evaluations of the relative benefits of each configuration and their sensitivity to design changes. The chosen parameters and their variation are shown in Table 1. The parameters involve geometric variables of blade radius, blade chord, blade twist, and duct thickness, and operating variables of tip Mach number and blade pitch.

Each design variable was varied independently and considered at hover and forward flight at ISA sea-level conditions. For hover conditions, the baseline configurations were trimmed to deliver the required thrust, about $T = 17,658$ N. For forward flight conditions, both configurations were considered in axial flight with a freestream Mach number of $Ma_\infty = 0.2$. Both initial configurations were trimmed to deliver 50% of the specified take-off thrust. Note that for all

Table 1 *Design variables for parametric study.*

Design Variable	Value		
	1	2	3
Tip Mach No. [-]	0.3	0.468	0.7
Pitch [$\Delta\%$]	-5	+5	+10
Blade Radius [m]	1.5	2.5	3.75
Blade Chord [$\Delta\%$]	-5	+5	+10
Blade Twist [$\Delta\%$]	-5	+5	+10
Duct Thickness [$\Delta\%$]	-5	+5	+10

other cases, the rotors were not trimmed, having the pitch angle of the baseline cases.

III. Computational Methods

A. The HMB3 Solver and CFD Simulation

High-fidelity CFD methods are used in the present work for the accurate prediction of ducted/un-ducted rotor aerodynamic performance and for the fine resolution of the near-field flowfields for further acoustic studies. The in-house Helicopter Multi-Block (HMB3) [18, 19] CFD code is used in the present work. The code has been widely used in simulations of rotorcraft flows [20–23]. HMB3 solves the Unsteady Reynolds Averaged Navier-Stokes (URANS) equations in integral form using the Arbitrary Lagrangian Eulerian (ALE) formulation for time-dependent domains, which may include moving boundaries. The Navier-Stokes equations are discretized using a cell-centered finite volume approach on multi-block, structured grids. The 3rd order MUSCL (Monotone Upstream-centered Schemes for Conservation Laws) approach is used to provide high-order accuracy in space. In the present work, simulations are performed with the $k - \omega$ SST [24] turbulence model.

To simplify the mesh generation process, the Chimera technique [25] was used to generate each grid component of the ducted and open rotor grids independently. The Chimera technique allows for overlapping and non-matching grids to be used. Field variables are interpolated from the components based on a predefined hierarchy. In the present analysis, each domain consisted of a background grid, a centrebody grid, a rotor grid and for the ducted rotor simulations, a duct grid.

For hover and forward flight simulations, the azimuthal symmetry of the configuration can be exploited, whereby only a fraction of the grid needs to be generated. The Rotating Reference Frame (RRF) method is implemented in HMB3 [16] for such simulations with rotational periodicity. The governing flow equations are reformulated and solved in a non-inertial rotating reference frame, which transforms the unsteady problem into steady calculations. Specially, for the simulation of ducted rotors as in this work, the stationary walls, e.g. the duct surfaces, are accounted for by imposing opposite motions in the rotating frame. For the unsteady simulations, the full grid is required. However, this

can simply be obtained by copying and rotating the grids of the steady simulations.

The background grid combines an O-grid topology in the azimuthal direction, with a H-grid topology in the vertical direction. The background grid was extended 4 rotor radii upstream, 8 rotor radii downstream and 4.5 radii in the radial direction, far enough to ensure no recirculation in the computational domain. The background grid was refined in the region of the rotor (and duct) and near wake regions and coarsened towards the far-field. Equally spaced cells were used in the azimuthal direction.

The rotor grid comprises a single blade constructed from a C-H topology. The rotor grid is refined in the near-wall region to ensure $y^+ \leq 1$. The duct grid is meshed as a Chimera component and is constructed using a C-H topology. Near-wall refinement is used to ensure $y^+ \leq 1$. The cell count away from the wall was defined by the chimera interpolation requirements between the rotor and background grids.

The same grid topologies and simulation strategies were used in previous studies of ducted/open rotors in Refs [13, 17], where grid sensitivity studies, using the same solver as this work, were also conducted. The grid sensitivity studies suggested that a total of about 12 million cells for one third of the computational domain would be more than adequate for mesh convergence. For the current hover and axial flight simulations, 22 million cells and 14 millions cells were used for the ducted and open configurations, respectively, for one forth of the computational domain. Each simulation required about 2800 cpu hours for the initial solution, but most successive simulations restarting from the initial solution needed only about 700 cpu hours.

HMB utility codes were used to assemble the full domain from the background grid and each Chimera component. The use of the Chimera technique to assemble each component allows further grid modifications to minimise the number of grids required for the parametric analysis. For unsteady simulations with non-axial inflows, the grids were copied and rotated to form the full domain.

B. Kriging Surrogate Model

The Kriging surrogate model [26] is a spatial interpolation method based on Gaussian regression. It predicts the value of an unobserved evaluation point using a distance-based function and a stochastic variance. Comparing to more conventional interpolation methods e.g. radial-base function or polynomial approximation, the benefit of Kriging approximation is that it provides not only predictions of function values at unobserved points, but also the uncertainty of the predictions. Kriging has hence been widely used in geostatics and aerodynamic shape optimisation studies. The drawback, however, is its large computational cost. This is because for each prediction, a linear system which scales with the number of sampling points must be solved.

In the current work, the Kriging model is used to help analyse results from the parametric study and to investigate the design sensitivities. Kriging approximations of the performance responses were created separately for each design variable in Table 1 using CFD results as the input sampling. In the present work, the Surrogate Modelling Toolbox of

Python [27] is used.

C. Far-field Acoustic Calculation

In the present work, the far-field acoustics is efficiently calculated using the FW-H equation [28], following the Farassat Formulation 1A [29], taking as input CFD solutions of the surface pressure fields. The formulation has been widely used for far-field noise predictions of aircraft, wind turbines [30], and coaxial propellers [31]. The Farassat Formulation 1A [29] solves surface terms of the FW-H equation, i.e. the thickness noise and the loading noise, in the time domain, by introducing the retarded time concept. The formulation results in two linear equations respectively, for the thickness and loading components.

The current far-field acoustic approach ignored the quadrupole source which requires costly integrations over volumes. This approach is reasonable, considering the subsonic nature of the current study, and is efficient and sufficiently accurate for purposes of engineering analysis based on CFD results. We have also assumed infinite duct impedance for simplification. Similar approaches were adopted for noise predictions for ducted fans [17, 32] and by Dighe et.al. [30] for ducted wind turbines. Additionally, the current implementation is an extension of the existing acoustic code HFWH (Helicopter Ffows Williams-Hawkings) [31] in the high-level Julia language. Extensive code-to-code comparisons have been performed in order to verify the current implementation. The required computational resources depend on the number of input panels and the signal length needed to be solved. For the current work, about 0.75 cpu hours were needed to solve for 1 second of the fly-by acoustic signal.

IV. Numerical Results

A. Numerical Validation

The HMB3 solver has been previously validated for a range of open rotor cases, e.g. Refs. [33–36]. It has also been used in previous simulation and optimisation studies of ducted rotors [13, 17]. The numerical validation and performance analysis of the baseline ducted rotor design in the current work, i.e. the ducted rotor configuration tested by Grunwald and Goodson [4] is only briefly discussed here. More detailed validation results and performance analyses at various operating conditions can be found in our previous work in Ref [13].

Key parameters of the ducted rotor configuration are presented in Figure 1. Note the aft section of the centrebody geometry is approximate, as no detailed data was given in the experiments [4]. The validation was performed at an advance ratio of $\mu = 0.191$. The Reynolds number based on the duct chord and the blade tip speed was 2.86 million and the flow was considered as fully turbulent in current simulations. The blade pitch at 75% blade radius was set at 29.58° . It should be noted that experiments reported a pitch of 24° . This pitch was initially examined by both CFD simulations and lower-order predictions, and yielded significantly lower thrust and torque. The current pitch of 29.58° was obtained using the lower-order code DFDC [11, 12] to match the experimental thrust by varying the blade pitch. However, the

lower-order code largely over-predicted the torque with the matched thrust. More details can be found in Ref [13]. The same operating conditions are also applied to the open rotor configuration with the duct removed to outline the performance differences.

Comparisons between experiments and HMB3 simulations, as well as, the breakdown of propulsion forces, are listed in Table 2. Good agreement between the HMB3 and test data can be noted. Note that all force and moment data were normalized using the far-field dynamic pressure, the duct chord length and the projected duct area (the product of duct exit diameter and duct chord). At this advance ratio ($\mu = 0.191$) and blade pitch, the ducted and un-ducted configurations produce similar amounts of total thrust, but the ducted rotor generates about 10% less torque and is hence slightly more efficient.

Table 2 *Aerodynamic loads breakdown and comparisons between experiments and HMB3 simulations of the Grunwald [4] configuration at $\mu = 0.191$.*

C_{F_x}	Experiments	Contribution	HMB3 Ducted Rotor	Contribution	HMB3 Open Rotor	Contribution
Total	1.40	100%	1.396	100%	1.355	100%
Rotor	1.00	71.4%	0.985	70.6%	1.418	104.7%
Duct(with CB)	0.40	28.5%	0.410	29.4%	-	-
centrebody	-	-	0.068	4.9%	-0.063	-4.7%
Rotor C_{M_x}	0.27	-	0.279	-	0.313	-
Efficiency η	0.713	-	0.687	-	0.594	-

B. Aerodynamic Performance of the Equivalent Rotors

Steady CFD computations were used to investigate these equivalent rotors at hover and axial forward flight conditions, whilst unsteady simulations were required for the yawed flight conditions. For the hover conditions, the rotors were trimmed to approximately the required thrust specified by the rotor scaling. The forward flight case was trimmed to approximately half of the value required under hover conditions. The pitch angle found for the forward flight case was also used for the yawed flight conditions. The required pitch angles, and corresponding thrust and torque for the equivalent rotors are presented in Table 3.

The hover case shows that both open and ducted rotors have been trimmed to similar values, closely matching the required thrust loading. However, the ducted rotor configuration required a notably higher blade pitch angle, resulting from the higher rotor inflow induced by the duct. Additionally, this resulted in a reduced torque output compared to the open rotor configuration.

For the forward flight case, the results are similar to that of the hover case, both configurations were trimmed to a similar value, approximately half the value at hover conditions. Again, whilst the ducted rotor required a higher pitch angle, the thrust was delivered with a reduced torque output. Note however that the power will be higher for the ducted

configuration due to the higher rotational speed required to have the same tip Mach number.

Table 3 *Computed loads for equivalent open and ducted rotor configurations.*

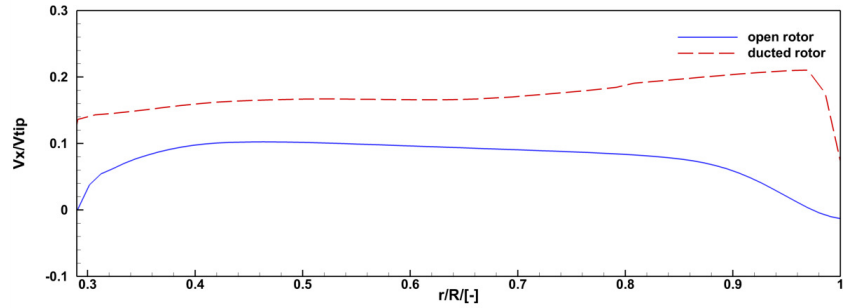
Configuration		Pitch Angle [°]	Thrust [kN]	Torque [kNm]
Hover	Open Rotor	5.25	18.3	6.76
	Ducted Rotor	13.0	18.9	5.41
Forward Flight	Open Rotor	27.3	8.73	18.2
	Ducted Rotor	37.3	9.05	14.7

Overall, the equivalent rotor concept has successfully demonstrated that ducting the rotor allows for the same thrust to be delivered with a significantly reduced tip radius (here, -40%) and frontal area (here, -75%). The ability to provide the same thrust for the reduced area results in part from the additional contribution to the thrust from the duct. For the hover case, the duct is found contributing to almost 50% of the thrust generation. On the other hand, for the forward flight case, the duct actually subtracts from the total thrust contribution, with the rotor providing almost all of the thrust. This is expected as the duct may contribute to drag at high advance ratios and low disk suction [4, 13]. For the forward flight case, the centre-body provides a small contribution to the thrust, whereas for the hover case, it has a negligible effect on the total thrust.

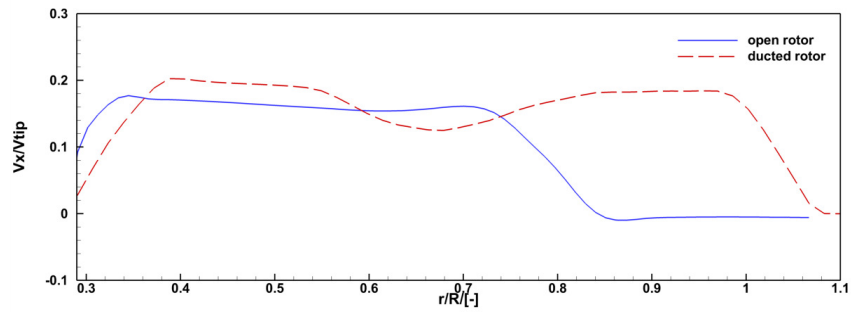
The inflow and wake profiles of the two configurations in hover, are also extracted and presented in Figures 3(a) and 3(b). For both configurations, the inflow profiles were extracted $0.25m$ upstream the rotor disk, while the wake profiles were extracted $2.5m$ downstream the rotor disk. As shown in Figure 3(a), the ducted rotor experienced higher inflow velocity, which is expected as the duct induces large inflow through the rotor disk. The wake profiles of the open rotor in Figure 3(b) show a typical wake contraction with the wake concentrating at about $r/R \leq 0.75$, or $R \leq 2.8m$. The wake of the ducted rotor is close to, but slightly stronger than that of the open rotor, resulting from the fact that the ducted configuration has a -40% reduced blade radius while producing the same thrust. No obvious wake contraction is noticed for the ducted rotor, which should be due to the duct diffuser effect. The ducted wake is quite evenly distributed within the blade radius, i.e. $R \leq 2.5m$, and gradually reduces to zero outwards. Overall, although at reduced blade radius and with higher inflow, the ducted configuration showed quite similar wake strength to the open rotor in hover.

Performance of the baseline equivalent designs were also examined at 20° yawed inflow at $Ma = 0.2$. The resolved flow-fields are shown in Figure 4(a) and 4(b). The open rotor wakes consists mostly of the tip vortices, while the duct circulation contributes the most to the ducted rotor wake at this yawed condition.

The unsteady loads at the non-axial inflow condition are shown in Figure 5. The aerodynamic forces are decomposed into propulsion components in the wind axis, while the torque is calculated in the axial direction. Both configurations delivered more lift than thrust. The open rotor experienced more variations in loads due to the axisymmetric inflow. On the other hand, the blades of the ducted rotor were offloaded and saw smaller variations in loads. The ducted rotor blades were producing thrust in the yawed condition, but the total thrust was negative due to the large negative contribution

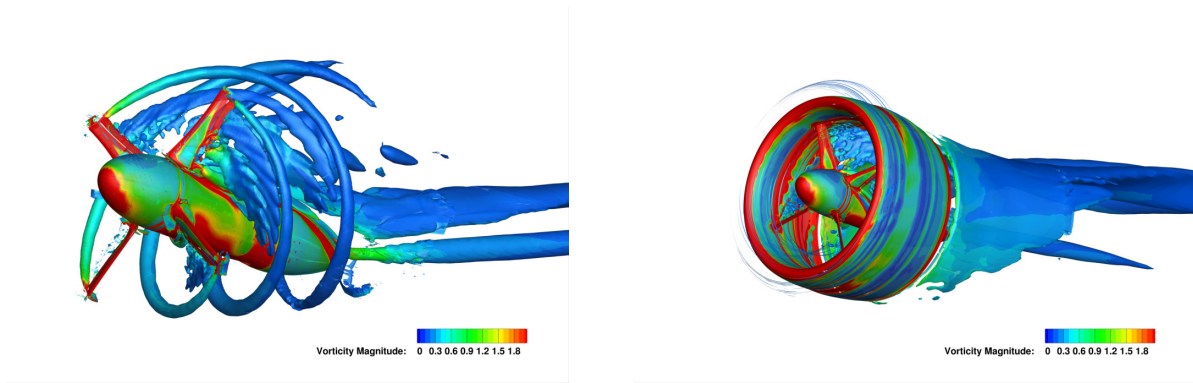


(a) Inflow profiles extracted $0.25m$ upstream the rotor disks.



(b) Wake profiles extracted $2.5m$ downstream the rotor disks, near the duct exit.

Fig. 3 Inflow and wake profiles of the ducted and open configurations in hover.



(a) Wake of the equivalent open rotor.

(b) Wake of the ducted rotor.

Fig. 4 Iso-surface of dimensionless Q-criterion=0.005 of the equivalent ducted/un-ducted rotors with 20° yawed inflow.

from the duct. Nonetheless, the ducted rotor produced large lifting forces with the major contribution from the duct. As for the torque, the rotors contributed the most in both configurations. The ducted rotor produced lower torque than the open rotor, with minor contributions from the duct.

C. Fly-by Noise of the 'Equivalent' Propulsors

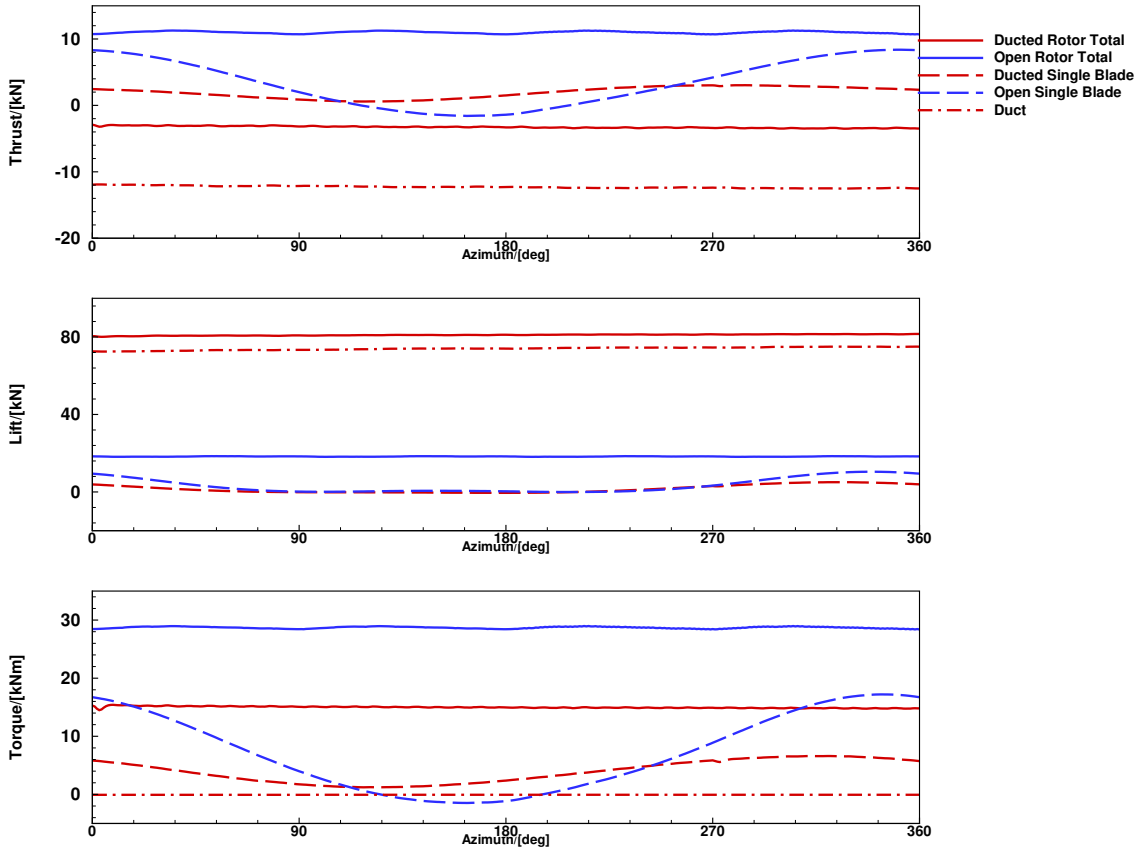


Fig. 5 Unsteady aerodynamic loads of ducted/un-ducted rotors with 20° yawed inflow. The forces are project in the wind direction.

The fly-by noise in the current work refers to the acoustic signals received at fixed ground microphones while the propulsors were flying overhead, in level flight. This scenario is often seen in aircraft noise certification. In the present work, the CFD solution was used as the input to the FW-H acoustic code. The calculations were performed assuming the two propulsor configurations are at the forward flight conditions of Table 3 at $Ma = 0.2$. The propulsors are assumed to be in level flight, $50m$ above ground. Three microphones were placed on the ground: one $50m$ to the port-side, one directly below the flight path, and the final one $50m$ to the starboard-side.

The computed acoustic signals of the two equivalent configurations are shown in Figure 6. Note that the ducted rotor was operating at a higher RPM to achieve the same tip speed as the larger-diameter open rotor, hence the frequency components are largely different. SPL values calculated using sound pressure signals within a rotor revolution are presented in Figure 7. For the open rotor, the acoustics is around 80 dB, with a slight increase near the rotor disk passage. For the ducted rotor, there is a low noise window slightly after the rotor disk passage for the ducted rotor, which is due to the duct shielding and the altered acoustic directivity. The duct tends to redirect the acoustic waves towards the axial direction [17]. This feature agrees well with our previous near-field acoustic study based on high-fidelity CFD

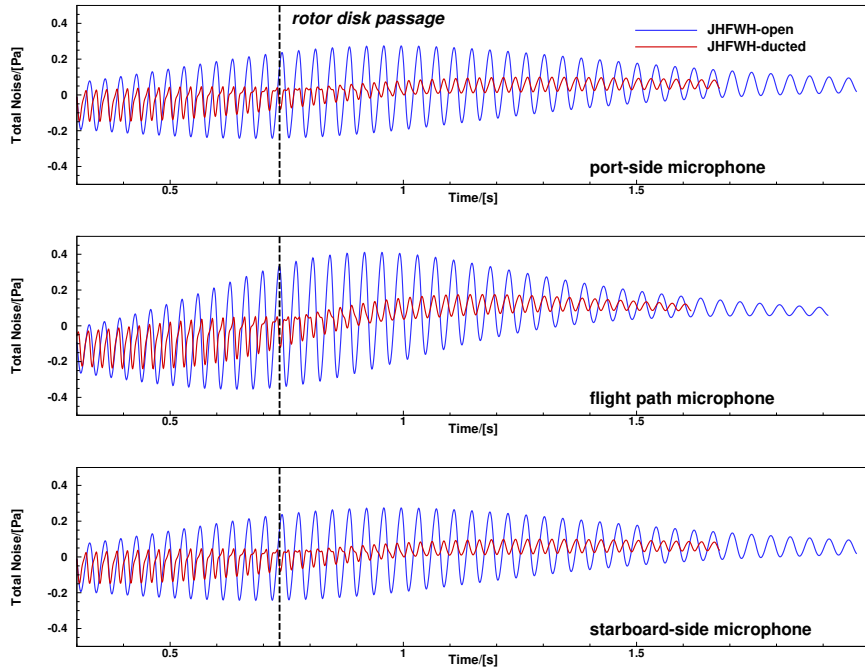


Fig. 6 Computed acoustic signals on the 3 ground microphones while the equivalent open and ducted configurations are flying by.

solutions [17]. As both rotors are moving further away, the acoustics becomes similar and reduces to around 75 dB. At the distance studied, the ducted configuration produces noise levels consistently lower and with a maximum reduction of about 15 dB comparing to the open rotor.

D. Parametric Study Results

First, a summary of the parametric study results, in terms of total thrust/power loadings in hover and forward flight, is shown in Figure 8. In general, the ducted rotor required slightly higher power than the equivalent open rotor for the same thrust, both in hover and in forward flight. This is because the ducted rotor has a higher RPM to have the same tip Mach number as the open rotor. The total thrust and power loadings of the ducted configuration are higher than the open rotor, due to the much reduced frontal area. For the current parametric study, the ducted/un-ducted configurations mostly showed consistent trends responding to the parametric variables. Variations in the tip Mach number caused significant changes in the thrust/power and the thrust/power loadings in both hover and forward conditions. Variations in the blade radius led to large thrust/power variations but had only a minor effect on the thrust/power loadings. Influences of the blade pitch are shown larger in forward flight than in hover for both thrust/power and their loadings. Responses to other parametric variables are relatively small around the initial point. Detailed discussion of the effect of each parameter follows.

Kriging curves have been fitted to the thrust, torque, and efficiency data to provide an impression of the response

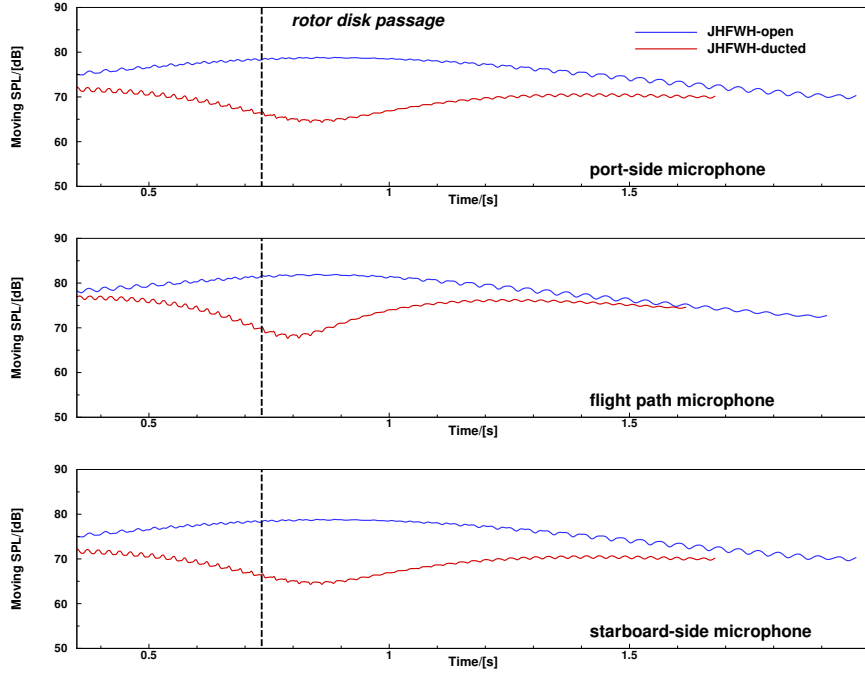


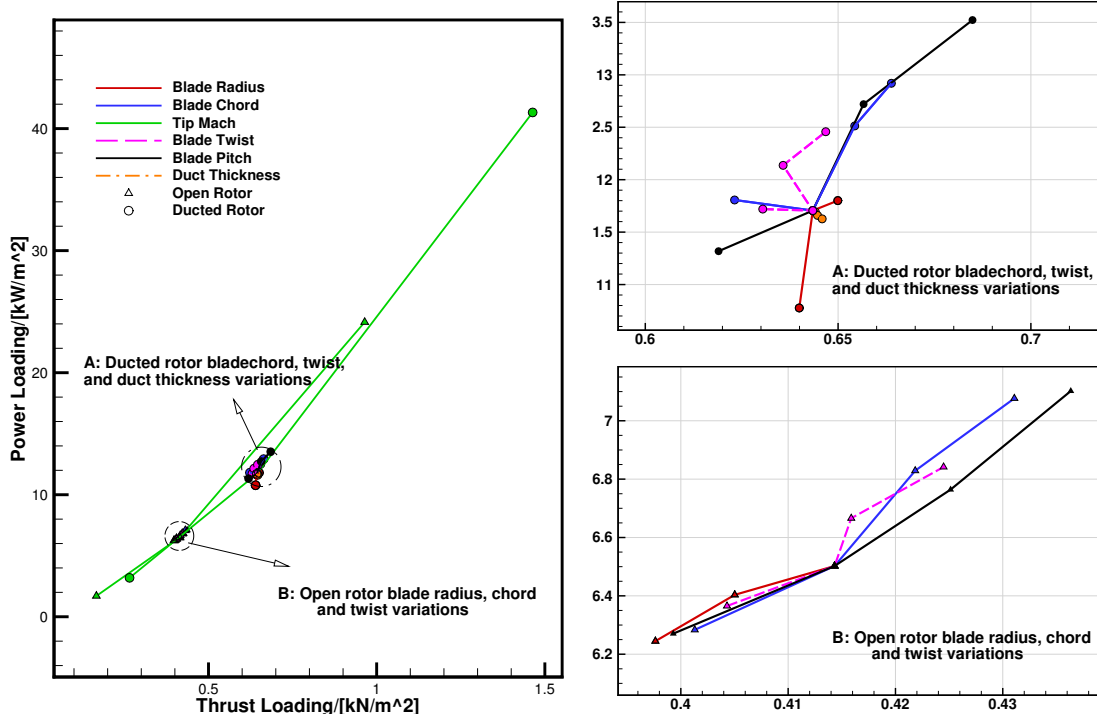
Fig. 7 Computed SPL values from the 3 ground microphones using signals within a rotor revolution while the equivalent open and ducted configurations are flying by.

of the configuration to the particular design change. For hover cases, the Figure of Merit (FoM) is used to measure the efficiency, while for forward flight cases, the Froude efficiency is used. For most cases in the present work, there are three design points in addition to the baseline. Also presented are the uncertainty quantification of the Kriging predictions. In general, it is noticed that the Kriging model gives more confident prediction for data interpolations rather than extrapolations.

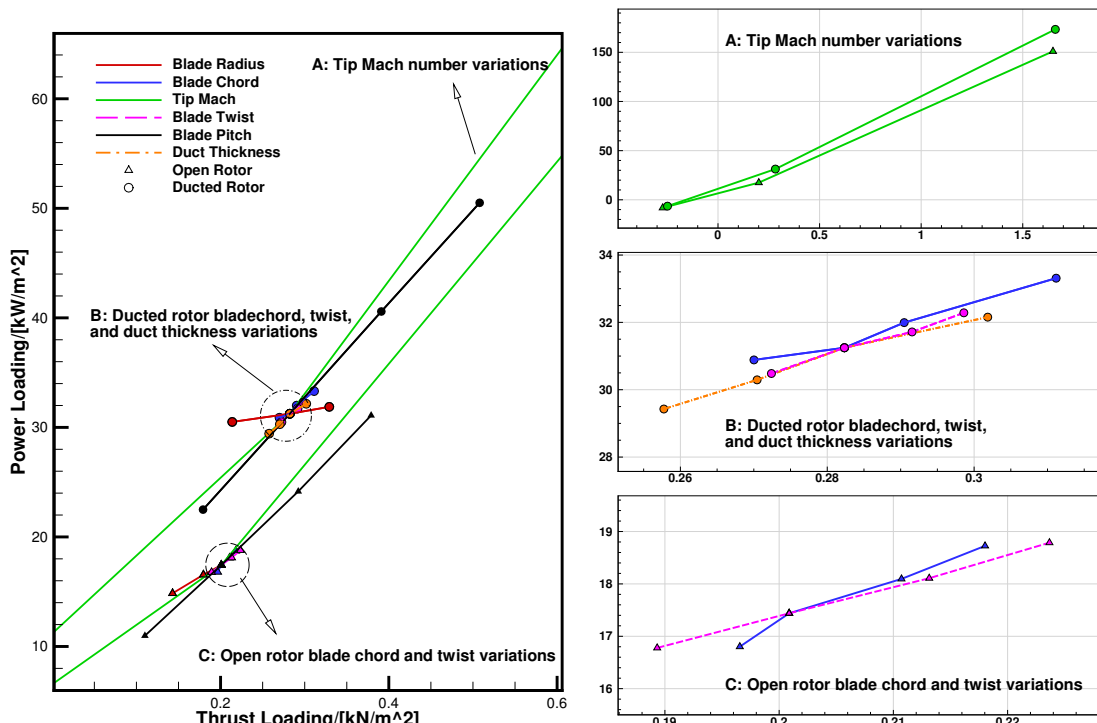
1. Tip Mach Number

The effect of tip Mach number was first studied. Figure 9 compares the computed loads for open and ducted rotors for the three tip Mach numbers studied at hover conditions. The dots denote the respective data sampling points evaluated by CFD computations, the lines denote the Kriging prediction, and the shaded area represent the 99% confidence interval. This notation applies to all following figures.

The open rotor configuration showed a significant variation on both thrust and torque with Tip Mach number. The change in tip Mach number resulted in significant changes in local angle of attack, thereby resulting in this significant variation. The Kriging curve shows a peak FoM around $Ma_{tip} = 0.6$. A similarly large variation in thrust and torque was also observed for the ducted rotor configuration in Figure 9(b). The Kriging curve shows the peak FoM lies at a tip Mach number a little higher than the baseline value. The ducted rotor configuration also showed a higher FoM than the open configuration, and at times higher than 1. This is because the total thrust is supported by the contribution from the



(a) Thrust loading-power loading map of the ducted/un-ducted rotors in hover.



(b) Thrust loading-power loading map of the ducted/un-ducted rotors in forward flight.

Fig. 8 Thrust loading-power loading map of the equivalent ducted/un-ducted rotors in hover and forward flight.

duct at no cost of torque. The breakdown of loads found that at lower tip speeds the total thrust was provided by the rotor. However, as the tip speed increased, the duct made an increasing contribution to the total thrust. This should be due to the larger rotor suction and hence the flow acceleration at the duct surface.

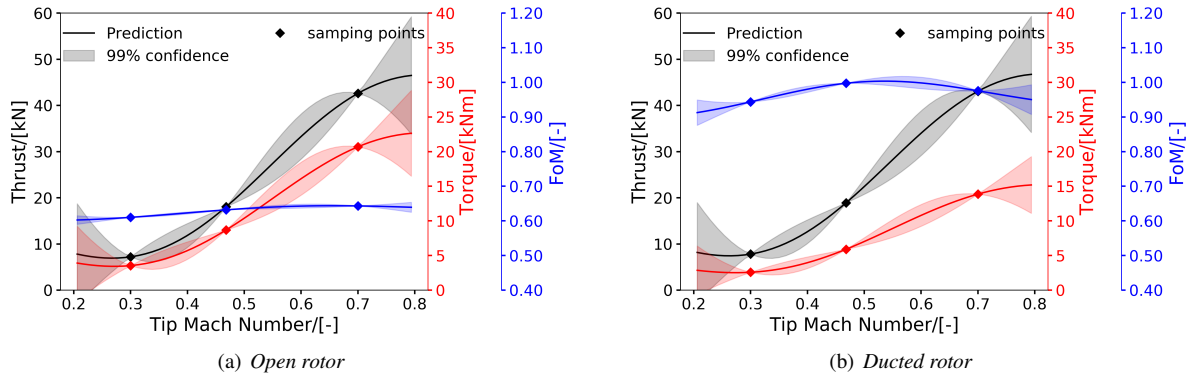


Fig. 9 Effect of tip Mach number on computed loading for open and ducted rotors with Kriging fitted for hover case.

The effect of tip speed was next evaluated at forward-flight conditions. Figure 10 presents the computed loading of both configurations with Kriging curve at forward flight conditions. Again, the tip Mach number was seen to have a significant effect on both open and ducted rotor configurations. For both configurations, without changing the blade pitch angle, reducing the tip speed below $Ma_{tip} = 0.3$ resulted in negative thrust values. This is typical as the local blade element may be facing negative effective angles of attack, due to the low rotational speed and the fast axial forward speed. On the other hand, as the tip speed increased, similarly to the hover case, there was a significant increase in the blade loads. The peak efficiency was predicted to occur near $Ma_{tip} = 0.6$ for both configurations. The ducted configuration shows generally lower efficiency than the equivalent open rotor in forward flight, due to the duct drag in forward flight. The efficiency of both configurations was set to zero below $Ma_{tip} = 0.3$ due to the negative thrust calculated at and below this point. The loads breakdown found that the open blades were more sensitive to tip Mach number changes. For the ducted configuration, the blade thrust changed significantly with tip speed variations, while the duct showed relatively small increases responding to the tip speed changes.

Overall, the tip Mach number had a significant effect on the resulting loads. Peak efficiency was observed for both configurations at both hover and forward flight conditions above the baseline value. However, the tip Mach number will also have a significant impact on the acoustic emissions of both configurations and must therefore be considered in the design choice.

2. Rotor Pitch

The blade pitch angle is typically used to trim the rotors to deliver the required thrust. As part of the parametric study, the rotor pitch angle for both open and ducted configurations was investigated. Figure 11 presents the computed

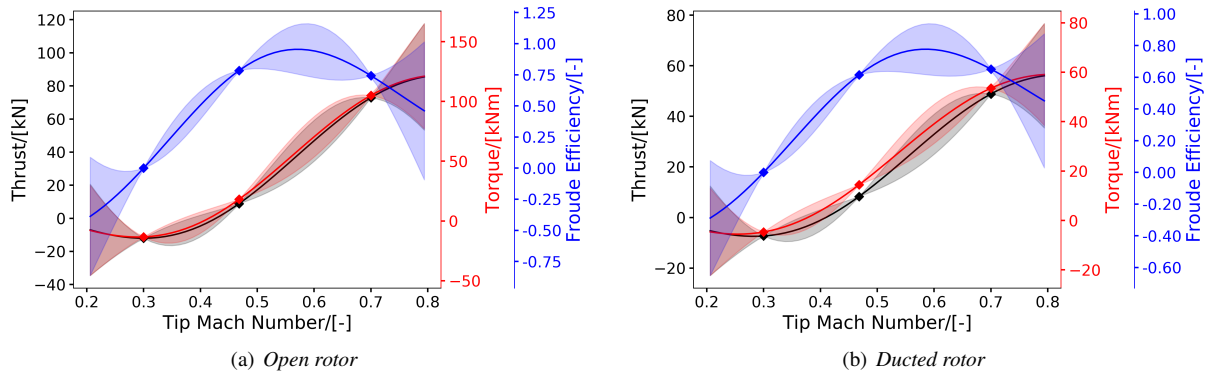


Fig. 10 Effect of tip Mach number on computed loading for open and ducted rotors with Kriging fitted for forward flight case.

performance of both configurations over a range of pitch angles at hover conditions.

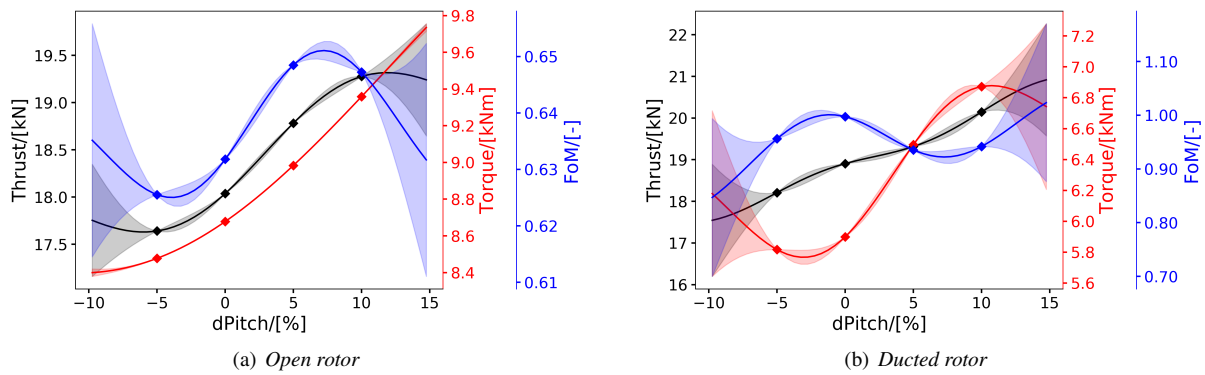


Fig. 11 Effect of blade pitch on computed loading for open and ducted rotors with Kriging fitted for hover case.

Both configurations showed the expected increase in both thrust and torque with increasing pitch angles. It should also be noted that the ducted configuration required a higher pitch angle to trim to the required thrust. Whilst the open rotor showed the greatest FoM near +5% pitch angles, but the absolute efficiency changes are generally minor. The ducted configuration had the peak FoM near the initial pitch angle. The Kriging curve has a sinusoidal shape and suggests that the efficiency may be further increased at higher pitch settings, yet this needs to be verified with more data points. Nonetheless, the FoM of the ducted configuration was greater than that of the open configuration over the range of pitch angles studied. The thrust breakdown found that open blade thrust was more sensitive to the pitch changes than the ducted blades. The duct thrust was also slightly increasing as the pitch angle was increased, which is due to the increased rotor suction.

Figure 12 evaluates the effect of pitch angle on both configurations at forward flight conditions. The forward flight conditions showed similar trends as those at hover conditions. For both configurations, the thrust and torque

were increasing almost linearly with the increasing pitch angle, which led to very small uncertainties in the Kriging approximation. For the open rotor configuration, there was a peak efficiency located near and beyond +5% pitch. Whilst for the ducted rotor, the peak efficiency was located beyond the positive range of pitch values. It is also worth noticing that as the pitch angle is increased, the ducted rotor efficiency becomes comparable to the open rotor in this forward flight condition. The thrust breakdown also found that the open blades are more sensitivities to pitch changes. The duct thrust was also increasing as the pitch angle was increased.

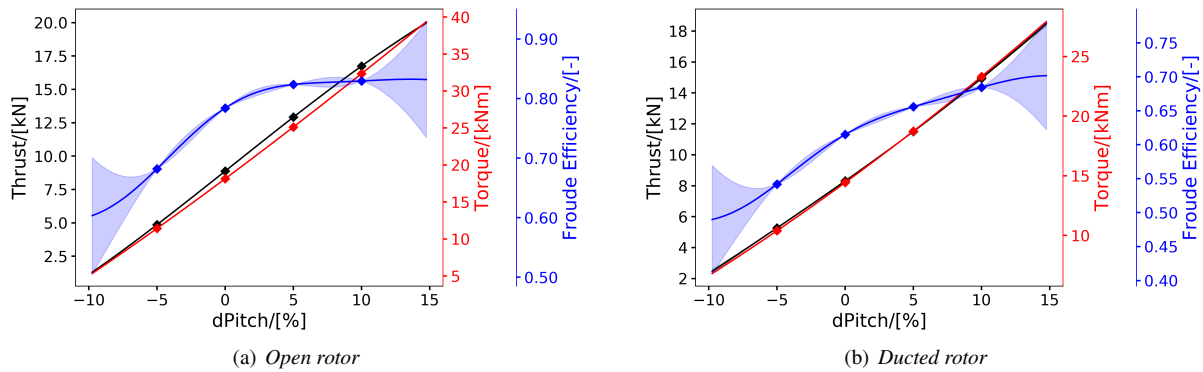


Fig. 12 Effect of blade pitch on computed loading for open and ducted rotors with Kriging fitted at forward flight conditions.

3. Blade Radius

The sensitivity of both configurations to the tip radius was next evaluated. In the present case, the tip speed was held constant (i.e. resulting in a change in rotational speed for each case), and the solidity was also held constant (i.e. resulting in scaling of the blade chord) for changes in the tip radius. In addition, the tip gap ratio between duct and rotor was also maintained, resulting in an increased duct radius for increasing rotor radius.

The open rotor configuration showed an increase in both thrust and torque for increasing radii in Figure 13(a). The ducted configuration in Figure 13(b) also showed an increase in loading for increasing radii. The increase in both thrust and torque was much more significant than that of the open rotor. Both configurations showed increased efficiency with increased radii. However, the efficiency of the ducted configurations varied very little and maintained near 1.0, while the open rotor efficiency varied between 0.5 to 0.65. The thrust breakdown of the ducted configuration found that the significantly higher thrust came from the additional contribution of thrust from the duct. In fact, the duct was found to produce an almost equal thrust to the open rotor configuration over the range of tip radii. At hover conditions, the ducted rotor was shown to be a much more effective propulsive device for increasing tip radii. The rotor of the ducted configuration produced higher thrust at increased radii compared to the open rotor when fixing the pitch and tip Mach number.

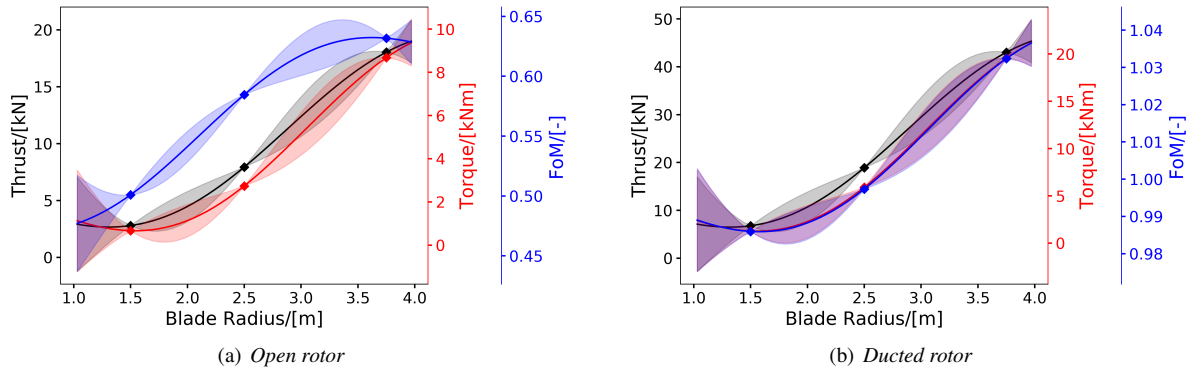


Fig. 13 Effect of tip radius on computed loading for open and ducted rotors with Kriging fitted for hover case.

The effect of blade radius was evaluated at forward flight conditions in Figure 14. The two configurations again showed very similar positive responses to the radius variations, with the ducted propeller having larger variations in the thrust and torque values. The efficiency of the two configurations are also similar in this forward flight condition. The thrust breakdown of the ducted configuration found that the ducted blades produced the majority of the thrust at this forward flight condition, while the duct contributed to an increasing amount of drag as the blade radius was increased. This is because the duct radius had to be increased to accommodate the increasing blade radius. Nonetheless, the rotor of the ducted configuration produced greater thrust for a given blade radius, than the equivalent open rotor.

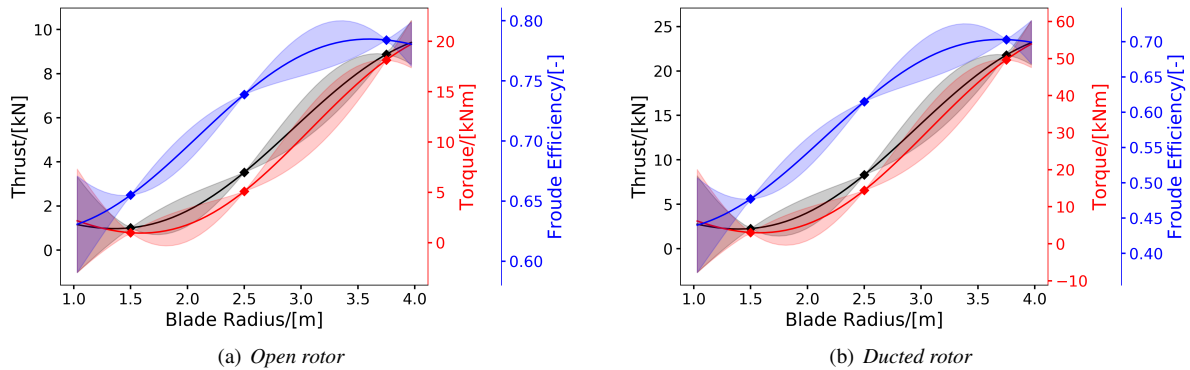


Fig. 14 Effect of blade radius on computed loading for open and ducted rotors with Kriging fitted for forward flight case.

Overall, the two configurations showed similar and positive responses to blade radius variations, but the ducted rotor configuration was shown to be more sensitive. Further, in hover conditions, the duct could produce as much thrust as the open rotor configuration. However, in forward flight this translated to an increase in drag. Therefore, the duct or rotor blade radius must be finely tuned for high performance across hover and forward flight operations.

4. Blade Chord

The rotor chord was investigated as a design choice on both configurations. The rotor chord was scaled over a range of values from the baseline. This affected the solidity of the rotor, which may also be indicative of changes in blade count and tip radius.

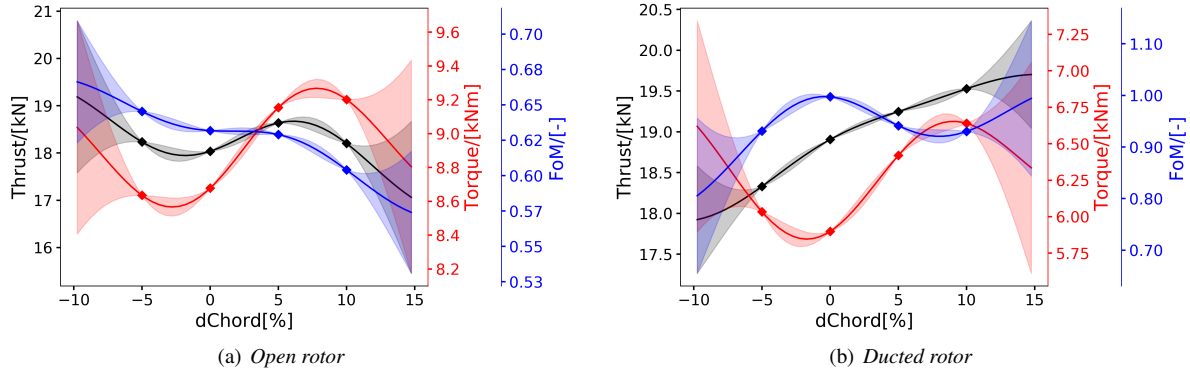


Fig. 15 Effect of blade chord on computed loading for open and ducted rotors with Kriging fitted for hover case.

Figure 15 presents the effect of chord variation on both open and ducted rotor configuration performance in hover. For both configurations, changes in the blade chord brought relatively small changes in the thrust and torque, but the performance variations tend to be wavy as suggested by the Kriging fitting. For the open rotor, the FoM was higher at reduced blade chords. For the ducted rotor, a peak FoM is observed near the baseline chord, but higher efficiency may be possible at larger chords as suggested by the Kriging fitting. Thrust breakdown of the ducted configuration found that the blade thrust was increasing with increasing chords, while the duct was found to deliver the peak thrust around the location of peak efficiency.

Figure 16 evaluates the effect of chord on both configurations at forward flight conditions. Both configurations showed consistently increasing loading with increased chord. However, in terms of efficiency, whilst the ducted configuration showed an increased propulsive efficiency with increased chord, the open configuration showed the opposite trend, although the absolute efficiency values varied little. Furthermore, the efficiency of the open configuration was greater than that of the ducted configuration across the range of blade chord values. No peak value was observed for either configuration, suggesting the optimal efficiency lies outwith the considered range. The thrust breakdown of the ducted configuration found that the change in chord had only a small effect on the duct. On the other hand, the change in chord shows the expected increase for the blade contribution.

Overall, the effect of chord was not consistent between hover and forward flight conditions, requiring a compromise in the design between the two conditions. However, at forward flight conditions, the effect of chord was found having a minimal effect on the duct performance, allowing for greater freedom in the design of the rotor.

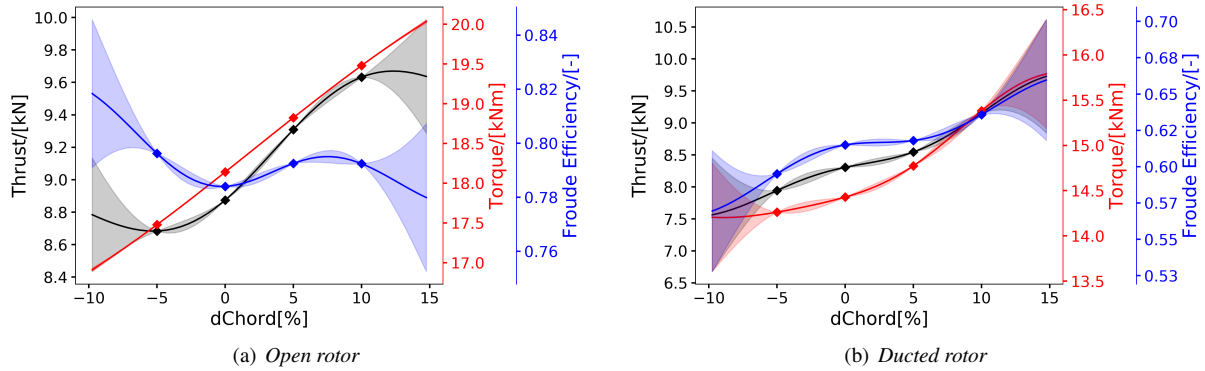


Fig. 16 Effect of blade chord on computed loading for open and ducted rotors with Kriging fitted for forward flight conditions.

5. Blade Twist

The rotor blade twist was next evaluated. The baseline case had a twist of about -23° . The twist was varied from the baseline for the current study.

The resulting loading for both open and ducted configurations was evaluated for hover conditions in Figure 17. For the open rotor, changes in the twist brought very little change in the thrust and torque values. Both thrust, torque, and efficiency were all found to increase with increasing twists. The open rotor efficiency also varied little around 0.64. For the ducted rotor, the variations in thrust and torque are also relatively small, and the trends are wavy. The ducted rotor efficiency experienced a slight variation near 0.95, with a peak FoM near the baseline twist.

The thrust breakdown of the ducted rotor found that the increased FoM can again be attributed to the contribution of the duct at hover conditions. Both the duct and blade were shown to have small but opposite responses to changes in twist around the baseline value. An overall small effect on the total ducted rotor thrust was resulted. Compared to the open configuration, the overall ducted rotor configuration hence had a reduced sensitivity to changes in blade twist.

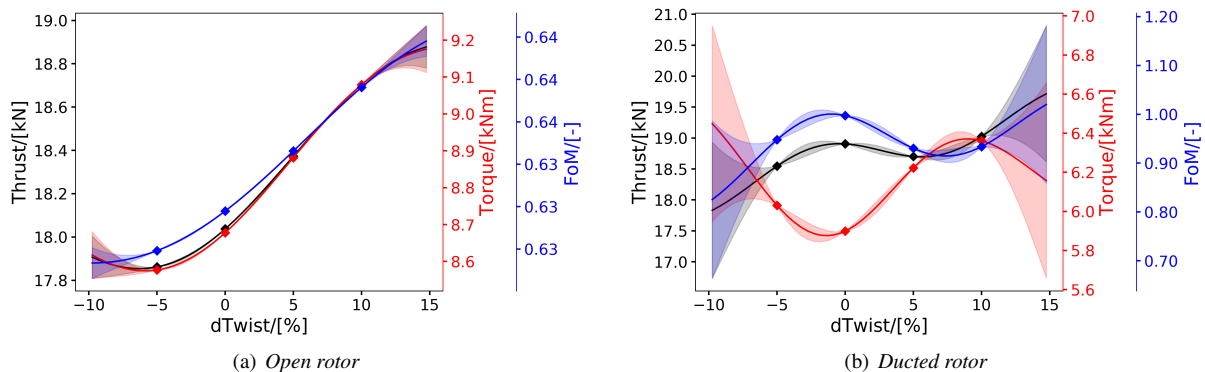


Fig. 17 Effect of blade twist on computed loading for open and ducted rotors with Kriging fitted for hover case.

Figure 18 evaluates the effect of blade twist now at forward flight conditions. Both open and ducted configurations showed increased loading with the increasing twist, with little uncertainties in the Kriging fitting. For the open rotor, the propulsive efficiency was shown to increase with increasing twist, with a possible peak value near +10% of the baseline design. For the ducted rotor configuration, the optimal value was also shown to be around +10% of the baseline design. The thrust breakdown of the ducted rotor found that the duct thrust was almost unchanged by the twist variations. The blade thrust variations were also small. Comparing the open configurations, the ducted configuration showed reduced sensitivity to the twist angle.

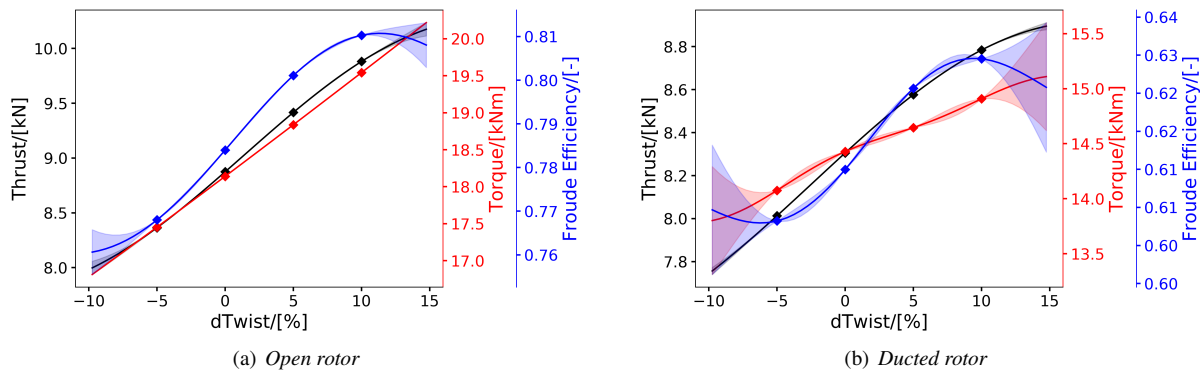


Fig. 18 Effect of blade twist on computed loading for open and ducted rotors with Kriging fitted for forward flight conditions.

Overall, both open and ducted configurations showed the expected increasing loading for increasing twist. Under both hover and forward flight conditions, the ducted configuration appeared less sensitive to changes in twist comparing to other design variables. This reduced sensitivity of the ducted configuration to the twist is beneficial, as more freedom

can be allowed in the blade twist.

6. Duct Thickness

The previous analysis has shown that the duct can have a significant affect on the ducted rotor performance at both hover and forward flight conditions. The duct thickness was included in the parametric study to evaluate further its impact on the ducted rotor configuration.

Figure 19(a) presents the effect on the ducted rotor performance over a range of duct thickness-chord ratios in hover. The performance of the ducted rotor was shown to be relatively unaffected by the duct thickness under hover conditions. The thrust breakdown found that both the rotor and duct thrust was relatively unaffected by changes in duct thickness. This is expected as the interior surface of the duct and the leading-edge region, which are responsible for the contribution to the total thrust in hover conditions, remained mostly unchanged by the thickness variation. Therefore, the duct thickness changes, which mostly alter the outer shapes, had little effect on the hover performance of the ducted rotor.

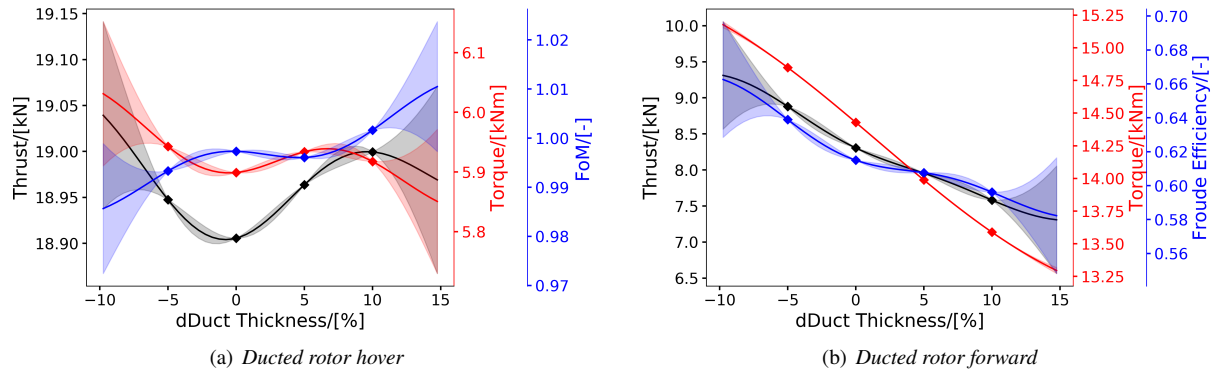


Fig. 19 Effect of duct thickness on computed loading for ducted rotor with Kriging fitted at hover and forward flight conditions.

The duct thickness was also examined at forward flight conditions as shown in Figure 19(b). The thrust, torque and resulting propulsive efficiency were all shown to degrade for increasing duct thickness. This is due to the increase in duct drag (negative thrust) with increasing thickness. However, a reduction in the rotor thrust was also observed, which should be due to induction changes brought by the duct shape variations.

The analysis shows that a duct with a much lower thickness would be optimal for the forward flight conditions. The hover analysis shows that this can be achieved with minimal impact on the hover performance.

V. Conclusions

In this work, we investigated the size correlation between the ducted rotor and the equivalent open rotor. A ducted rotor design and the equivalent open rotor were proposed to support a four-rotor vehicle of 6,000 kg, based on a model-size NASA ducted rotor test case. The aerodynamic and far-field acoustic performance of the baseline designs was examined and compared using modern CFD methods. A parametric study was performed to investigate performance variations with respect to changes in geometric and operating parameters of the equivalent rotors. Kriging-based surrogate models were built to further inspect the performance variations to particular design changes. From the current study, the following conclusions can be derived:

- 1) A pair of equivalent ducted/un-ducted rotor designs were proposed using the momentum theory and BEMT methods. The ducted rotor was able to deliver the desired thrust in hover and in forward flight at the cost of much lower torque, but the power requirement was slightly higher due to the higher RPM. In hover, the ducted rotor showed a higher FoM due to the duct thrust. The wake profiles of the two configurations in hover were also found similar, although the ducted rotor has a much reduced radius while producing the same thrust. In the forward flight case tested, however, the ducted rotor showed lower efficiency than the equivalent open rotor due to the duct drag. Compared to the equivalent open rotor, the ducted rotor has a 40% reduced radius and a

70% reduced frontal area, which is very favourable for confined space. Far-field acoustic calculations of the two configurations using the FW-H equations also showed great acoustic benefits by ducting, despite the higher RPM of the ducted rotor.

- 2) For the non-axial flight condition examined, the equivalent rotors contributed more to the lift than to the thrust. The ducted blades were offloaded and experienced lower variations in loads caused by the asymmetric inflow, thanks to the duct shielding. The duct surface produced large forces due to the non-axial free-stream. The ducted rotor configuration produced negative thrust at the condition examined, due to the large negative contributions from the duct. However, the ducted lifting force was about 3 times higher than that of the open rotor, with the major contribution from the duct.
- 3) A parametric study of the equivalent ducted/un-ducted rotors was performed in hover and in forward flight, and Kriging-based surrogate models were built to inspect the performance trends subject to the design changes. The ducted rotor showed higher thrust and power loadings due to the smaller size. The tip Mach number shows significant effects on the aerodynamic loads. Peak efficiencies were observed for both configurations at both hover and forward flight conditions above the baseline tip Mach number. Increasing the blade pitch leads to increased loadings for both configurations, but optimal efficiencies were noted at specific pitch setting. For the ducted rotor in forward flight, its efficiency can be higher than the open rotor when the pitch angles are large. The ducted rotor configuration is shown to be more sensitive to changes in tip radius. For hover conditions, the enlarged duct alone could produce as much thrust as the open rotor configuration. However, in forward flight, the enlarged duct contributed largely to drag. Effects of chord are not consistent between hover and forward flight conditions for both configurations, hence requiring a compromise in the design between the two conditions. However, at forward flight conditions, the effect of chord is shown to have a minimal effect on the duct performance. Both open and ducted configurations showed the expected increasing loading for increasing twist. Under both hover and forward flight conditions, the ducted configuration appears less sensitive to changes in twist. The duct thickness shows minor effects on hover performance, but lower thickness would be beneficial for the forward flight.

Future work will continue to investigate performance comparisons of the equivalent ducted/un-ducted rotors at further operating conditions. We are also working to develop efficient acoustic methods to account for the quadrupole noise, duct lining, impedance, and internal structures.

Acknowledgments

The joint sponsorship of the University of Glasgow and the China Scholarship Council is gratefully acknowledged. Dr Dale Smith was funded by the Leonardo Helicopters during this project.

References

- [1] Filippone, A., and Barakos, G., “Rotorcraft systems for urban air mobility: A reality check,” *The Aeronautical Journal*, Vol. 125, No. 1283, 2021, pp. 3–21. <https://doi.org/https://doi.org/10.1017/aer.2020.52>.
- [2] Zhang, T., and Barakos, G., “Review on Ducted Fans for Compound Rotorcraft,” *The Aeronautical Journal*, Vol. 124, No. 1277, 2020, pp. 941–974. <https://doi.org/https://doi.org/10.1017/aer.2019.164>.
- [3] Grunwald, K. J., and Goodson, K. W., “Division of aerodynamic loads on a semispan tilting-ducted-propeller model in hovering and transition flight,” Tech. rep., NASA TN D-1257, 1962.
- [4] Grunwald, K. J., and Goodson, K. W., “Aerodynamic Loads on an Isolated Shrouded-propeller Configuration for Angles of Attack from -10 Deg to 110 Deg,” *NASA TN D-995*, 1962.
- [5] Mort, K. W., and Gamse, B., “A wind-tunnel investigation of a 7-foot-diameter ducted propeller,” Tech. rep., NASA-TN-D-4142, 1967.
- [6] Martin, P., and Tung, C., “Performance and flowfield measurements on a 10-inch ducted rotor vtol uav,” Tech. rep., Army Research Development and Engineering Command, Moffett Field CA, Aviation Aeroflight Dynamics Directorate, 2004.
- [7] Akturk, A., and Camci, C., “Experimental and computational assessment of a ducted-fan rotor flow model,” *Journal of Aircraft*, Vol. 49, No. 3, 2012, pp. 885–897. <https://doi.org/https://doi.org/10.2514/1.C031562>.
- [8] Yilmaz, S., Erdem, D., and Kavsaoglu, M., “Effects of Duct Shape on a Ducted Propeller Performance,” *51st AIAA Aerospace Sciences Meeting including the New Horizons Forum and Aerospace Exposition*, 2013, p. 803. <https://doi.org/10.2514/6.2013-803>.
- [9] Hubbard, H. H., “Sound measurements for five shrouded propellers at static conditions,” Tech. rep., NACA-TN-2024, 1950.
- [10] Malgoezar, A. M., Vieira, A., Snellen, M., Simons, D. G., and Veldhuis, L. L., “Experimental characterization of noise radiation from a ducted propeller of an unmanned aerial vehicle,” *International Journal of Aeroacoustics*, Vol. 18, No. 4-5, 2019, pp. 372–391. <https://doi.org/https://doi.org/10.1177/1475472X19852952>.
- [11] Youngren, H., Drela, M., and Sanders, S., “Ducted Fan Design Code,” , 2005. URL <http://web.mit.edu/drela/Public/web/dfdc/>, available online, retrieved 07-06-2021.
- [12] Drela, M., and Youngren, H., “Axisymmetric Analysis and Design of Ducted Rotors,” , 2005. URL <http://web.mit.edu/drela/Public/web/dfdf/>, available online, retrieved 07-06-2021.
- [13] Zhang, T., and Barakos, G. N., “High-Fidelity CFD Validation and Assessment of Ducted Propellers for Aircraft Propulsion,” *Journal of the American Helicopter Society*, Vol. 66, No. 1, 2021, pp. 1–28. <https://doi.org/10.4050/JAHS.66.012008>.
- [14] Bontempo, R., and Manna, M., “Solution of the flow over a non-uniform heavily loaded ducted actuator disk,” *Journal of Fluid Mechanics*, Vol. 728, 2013, pp. 163–195. <https://doi.org/https://doi.org/10.1017/jfm.2013.257>.

- [15] Jimenez, B. G., and Singh, R., “Effect of duct-rotor aerodynamic interactions on blade design for hover and axial flight,” *53rd AIAA Aerospace Sciences Meeting*, 2015, p. 1030. <https://doi.org/10.2514/6.2015-1030>.
- [16] Biava, M., and Barakos, G. N., “Optimisation of ducted propellers for hybrid air vehicles using high-fidelity CFD,” *The Aeronautical Journal*, Vol. 120, No. 1232, 2016, pp. 1632–1657. <https://doi.org/https://doi.org/10.1017/aer.2016.78>.
- [17] Zhang, T., and Barakos, G. N., “High-fidelity numerical analysis and optimisation of ducted propeller aerodynamics and acoustics,” *Aerospace Science and Technology*, Vol. 113, 2021, p. 106708. <https://doi.org/https://doi.org/10.1016/j.ast.2021.106708>.
- [18] Steijl, R., Barakos, G., and Badcock, K., “A Framework for CFD Analysis of Helicopter Rotors in Hover and Forward Flight,” *International Journal for Numerical Methods in Fluids*, Vol. 51, No. 8, 2006, pp. 819–847. <https://doi.org/10.1002/flid.1086>.
- [19] Biava, M., Woodgate, M., and Barakos, G. N., “Fully implicit discrete-adjoint methods for rotorcraft applications,” *AIAA Journal*, Vol. 54, No. 2, 2015, pp. 735–749. <https://doi.org/https://doi.org/10.2514/1.J054006>.
- [20] Antoniadis, A., Drikakis, D., Zhong, B., Barakos, G., Steijl, R., Biava, M., Vigevano, L., Brocklehurst, A., Boelens, O., Dietz, M., et al., “Assessment of CFD methods against experimental flow measurements for helicopter flows,” *Aerospace Science and Technology*, Vol. 19, No. 1, 2012, pp. 86–100. <https://doi.org/https://doi.org/10.1016/j.ast.2011.09.003>.
- [21] Steijl, R., and Barakos, G., “CFD analysis of complete helicopter configurations—lessons learnt from the GOAHEAD project,” *Aerospace Science and Technology*, Vol. 19, No. 1, 2012, pp. 58–71. <https://doi.org/https://doi.org/10.1016/j.ast.2011.01.007>.
- [22] Han, D., Patrikakis, V., and Barakos, G. N., “Helicopter flight performance improvement by dynamic blade twist,” *Aerospace Science and Technology*, Vol. 58, 2016, pp. 445–452. <https://doi.org/https://doi.org/10.1016/j.ast.2016.09.013>.
- [23] Garcia, A. J., and Barakos, G. N., “Numerical simulations on the ERICA tiltrotor,” *Aerospace Science and Technology*, Vol. 64, 2017, pp. 171–191. <https://doi.org/https://doi.org/10.1016/j.ast.2017.01.023>.
- [24] Menter, F. R., “Two-equation eddy-viscosity turbulence models for engineering applications,” *AIAA Journal*, Vol. 32, No. 8, 1994, pp. 1598–1605. <https://doi.org/10.2514/3.12149>.
- [25] Jarkowski, M., Woodgate, M. A., Barakos, G. N., and Rokicki, J., “Towards Consistent Overset Mesh Methods for Rotorcraft CFD,” *International Journal for Numerical Methods in Fluids*, Vol. 74, 2014, pp. 543–576. <https://doi.org/10.1002/flid.3861>.
- [26] Sacks, J., Schiller, S. B., and Welch, W. J., “Designs for Computer Experiments,” *Technometrics*, Vol. 31, No. 1, 1989, pp. 41–47. <https://doi.org/10.1080/00401706.1989.10488474>.
- [27] Bouhlel, M. A., Hwang, J. T., Bartoli, N., Lafage, R., Morlier, J., and Martins, J. R., “A Python surrogate modeling framework with derivatives,” *Advances in Engineering Software*, Vol. 135, No. 2018, 2019. <https://doi.org/10.1016/j.advengsoft.2019.03.005>.
- [28] Ffowcs Williams, J. E., and Hawkins, D. L., “Sound generation by turbulence and surfaces in arbitrary motion,” *Philosophical Transactions of the Royal Society of London. Series A, Mathematical and Physical Sciences*, Vol. 264, No. 1151, 1969, pp. 321–342. <https://doi.org/https://doi.org/10.1098/rsta.1969.0031>.

- [29] Farassat, F., "Derivation of Formulations 1 and 1A of Farassat," Tech. rep., NASA / TM-2007-214853, 2007.
- [30] Dighe, V. V., Avallone, F., and van Bussel, G., "Effects of yawed inflow on the aerodynamic and aeroacoustic performance of ducted wind turbines," *Journal of Wind Engineering and Industrial Aerodynamics*, Vol. 201, 2020, p. 104174. <https://doi.org/https://doi.org/10.1016/j.jweia.2020.104174>.
- [31] Smith, D. A., Filippone, A., and Bojdo, N., "Noise reduction of a Counter Rotating Open Rotor through a locked blade row," *Aerospace Science and Technology*, Vol. 98, No. 105637, 2020. <https://doi.org/10.1016/j.ast.2019.105637>.
- [32] Luo, B., Chu, W., and Zhang, H., "Tip leakage flow and aeroacoustics analysis of a low-speed axial fan," *Aerospace Science and Technology*, 2020, p. 105700. <https://doi.org/https://doi.org/10.1016/j.ast.2020.105700>.
- [33] Smith, D. A., Filippone, A., and Barakos, G. N., "Acoustic Analysis of Counter-Rotating Open Rotors with a Locked Blade Row," *AIAA Journal*, 2020. <https://doi.org/10.2514/1.J059273>.
- [34] Jimenez-Garcia, A., Barakos, G. N., and Gates, S., "Tiltrotor CFD Part I - Validation," *Aeronautical Journal*, Vol. 121, No. 1239, 2017, pp. 577–610. <https://doi.org/10.1017/aer.2017.17>.
- [35] Chirico, G., Barakos, G. N., and Bown, N., "Numerical aeroacoustic analysis of propeller designs," *Aeronautical Journal*, Vol. 122, No. 1248, 2018, pp. 283–315. <https://doi.org/10.1017/aer.2017.123>.
- [36] Barakos, G. N., and Johnson, C. S., "Acoustic comparison of propellers," *International Journal of Aeroacoustics*, Vol. 15, No. 6-7, 2016, pp. 575–594. <https://doi.org/10.1177/1475472X16659214>.